

# Ultra-Stable Cycling of High Capacity Room Temperature Sodium-Sulfur Batteries Based on Sulfurated Poly(acrylonitrile)

Saravanakumar Murugan,<sup>[a]</sup> Stefan Niesen,<sup>[a]</sup> Julian Kappler,<sup>[a]</sup> Kathrin Küster,<sup>[b]</sup> Ulrich Starke,<sup>[b]</sup> and Michael R. Buchmeiser<sup>\*[a, c]</sup>

We report on a room temperature (RT) sodium-sulfur (Na–S) battery based on a sodium anode, a sulfurated poly(acrylonitrile) (SPAN) cathode and an electrolyte containing sodium tetrakis(hexafluoroisopropoxy) borate ( $\text{Na}[\text{B}(\text{hfip})_4]$ ; hfip=hexafluoroisopropoxide) in a mixture of ethylene carbonate (EC), dimethyl carbonate (DMC) and fluoroethylene carbonate (FEC). The hfip anion as a weakly coordinating anion (WCA) provides high anodic stability, high ionic conductivity, and superior electrochemical performance in carbonate-based solvents. The Na-SPAN cell exhibits an initial discharge capacity

of  $1360 \text{ mAh g}_s^{-1}$  and a remarkable reversible capacity of  $1072 \text{ mAh g}_s^{-1}$  after 1000 cycles at  $3 \text{ C}$  ( $C=C$ -rate,  $5.025 \text{ A g}_s^{-1}$ ) with an insignificant average capacity decay of less than  $0.021\%$  per cycle. A careful choice of the discharge cut-off potential (DCP) reveals that a DCP of  $0.2 \text{ V}$  allows for stable cycling for more than 500 cycles while a DCP of  $0.5 \text{ V}$  results in a constant capacity decay. The excellent cycle stability at a DCP of  $0.2 \text{ V}$  is likely to be caused by the high conversion of the SPAN-bound sulfur into  $\text{Na}_2\text{S}$ .

## 1. Introduction

To date, lithium-ion batteries are widely used for energy storage in portable electronic devices and electric vehicles.<sup>[1–2]</sup> Apart from the growing electric vehicle market, lithium-ion batteries are also increasingly employed in large-scale stationary energy storage applications. In view of that, new materials with high energy density and good cycle stability that can be produced at low costs are of significant importance. Therefore, the use of inexpensive and environmentally benign materials such as sodium and sulfur has attracted substantial interest in recent years. Particularly the raw material costs of lithium compared to sodium ( $25000 \text{ \$/ton}$  vs.  $2100 \text{ \$/ton}$ ), a consequence of the natural abundance of these metals in the earth's crust (Li:  $20 \text{ mg kg}^{-1}$ ; Na:  $28400 \text{ mg kg}^{-1}$ ), makes sodium an economic choice for electrode materials.<sup>[3–5]</sup>

Sulfur is a low-cost, highly abundant raw material with a high theoretical capacity of  $1675 \text{ mAh g}_s^{-1}$ . Consequently, high-

temperature (HT) Na–S batteries based on a solid-state  $\beta$ -alumina electrolyte are already widely used in energy storage for large-scale grid applications.<sup>[1,6]</sup> Such batteries are operated at  $300\text{--}350^\circ\text{C}$  to ensure adequate conductivity of the electrolyte and contain both Na and S in the molten state. Clearly, the use of such batteries entails severe disadvantages such as increased safety risks and the presence of corrosive polysulfides.<sup>[7]</sup> Therefore, room temperature (RT) Na–S batteries have moved into the center of interest. However, RT Na–S batteries so far suffered from a severe capacity decay due to the formation of soluble polysulfides in the electrolyte, which shuttle to the anode.<sup>[8]</sup>

Cathode materials, which avoid polysulfide shuttling such as sulfurated poly(acrylonitrile) (SPAN), have been developed by Wang et al. and show excellent performance in lithium-sulfur batteries using a carbonate-based electrolyte.<sup>[9]</sup> The structure and electrochemistry of SPAN within the context of Li–S batteries have been studied in detail.<sup>[10–17]</sup> By contrast, the use of SPAN for RT Na–S batteries so far resulted in limited success. Though a remarkable initial discharge capacity of  $655 \text{ mAh g}_{cathode}^{-1}$  was observed, however, it dropped to  $500 \text{ mAh g}_{cathode}^{-1}$  within 20 cycles.<sup>[18]</sup>

Until now, various salts and different combinations of ether and/or carbonate-based solvents have been used for RT Na–S batteries. The choice of electrolyte highly depends on the compatibility with the sodium electrode. Since sodium is highly reactive and forms an unstable solid electrolyte interface (SEI) layer by reacting with the electrolyte, the choice of electrolyte is crucial. So far, sodium salts such as commercially available  $\text{NaPF}_6$ ,  $\text{NaTFSI}$ ,  $\text{NaClO}_4$ ,  $\text{NaFSI}$ , and  $\text{NaBF}_4$  (TFSI=bis(trifluoromethylsulfon)imide; FSI=bis(fluoromethylsulfon)imide) have been used for Na–S cells.<sup>[19]</sup> Even though weakly coordinating anions (WCAs) possess a wide potential window,

[a] S. Murugan, S. Niesen, J. Kappler, Prof. M. R. Buchmeiser  
Institute of Polymer Chemistry  
University of Stuttgart  
70569 Stuttgart, Germany

[b] K. Küster, Prof. U. Starke  
Max Planck Institute for Solid State Research  
70569 Stuttgart, Germany

[c] Prof. M. R. Buchmeiser  
German Institutes of Textile and Fiber Research (DITF) Denkendorf  
73770 Denkendorf, Germany  
E-mail: michael.buchmeiser@ipoc.uni-stuttgart.de

 Supporting information for this article is available on the WWW under  
<https://doi.org/10.1002/batt.202100125>

 © 2021 The Authors. *Batteries & Supercaps* published by Wiley-VCH GmbH. This is an open access article under the terms of the Creative Commons Attribution License, which permits use, distribution and reproduction in any medium, provided the original work is properly cited.

high ionic conductivity and allow for high coulombic efficiency, they have been limited so far to Li and Mg batteries.<sup>[20–25]</sup> In view of the attractiveness of WCAs and SPAN as a cathode material, we were interested in the question of whether Na fluoroalkoxy borates, which have been reported to be stable against moisture and have high ionic conductivity as well as low viscosity,<sup>[26–27]</sup> would allow for creating long-time stable Na–S cells. To the best of our knowledge, the concept of using fluoroalkoxy borates as WCAs in combination with SPAN for RT Na–S batteries has not been reported so far. And indeed, the use of sodium tetrakis(hexafluoroisopropoxy) borate ( $\text{NaB}[\text{hfip}]_4$ ) in a mixture of ethylene carbonate (EC), dimethyl carbonate (DMC), and fluoroethylene carbonate (FEC) results in an electrolyte with high room temperature ionic conductivity ( $6.135 \text{ mS cm}^{-1}$ ). Variations in the discharge cut-off potential (DCP) provide valuable insights into the cycle stability of the cell. Cyclic voltammetry (CV), galvanostatic intermittent titration technique (GITT), and X-ray photoelectron spectroscopy (XPS) reveal that a DCP of 0.2 V allows for maintaining a stable discharge capacity by promoting the formation of  $\text{Na}_2\text{S}$  and reducing the formation of nucleophilic oligosulfides ( $\text{S}_2^{2-}$ ), thereby suppressing their reaction with carbonate-based solvents.<sup>[28]</sup>

## 2. Results and Discussion

### 2.1. Electrochemical Stability of the Electrolyte

$\text{Na}[\text{B}(\text{hfip})_4]3\text{DME}$  (DME = 1,2-dimethoxyethane) was synthesized as described in the literature.<sup>[27]</sup> Its purity was confirmed by  $^1\text{H}$  and  $^{19}\text{F}$  nuclear magnetic resonance (NMR) and by combustion elemental analysis (Figure S1, S2, Table S1). 1 M  $\text{Na}[\text{B}(\text{hfip})_4]$  in EC : DMC (1:1) + 13 wt. % FEC was chosen as electrolyte. FEC can form a NaF-rich, stable SEI on Na, which prevents further electrolyte decomposition and allows dendrite-free cycling.<sup>[29]</sup> Furthermore, FEC has lower binding energy with sodium polysulfides and can thus suppress polysulfide shuttling.<sup>[30]</sup> The electrolyte was tested for its stability vs. oxidation with different current collectors to identify the potential window within which the cells could be cycled.<sup>[31–32]</sup> Results from linear sweep voltammetry (LSV) of different working electrodes such as carbon-coated aluminum (typically used as a current collector for sulfur cathodes), copper, and platinum are shown in the I–U polarization curve (Figure 1). While the decomposition of the electrolyte on copper started at 3.21 V, the electrolyte was stable up to 4.65 V and 4.6 V using Pt and carbon-coated Al, respectively, demonstrating the compatibility of the electrolyte with conventional Al current collectors.

### 2.2. Electrochemical Performance

Since the sulfur is covalently bound to the carbon backbone in SPAN, long-chain polysulfide dissolution, which is responsible for the polysulfide shuttle effect and capacity fading, can be

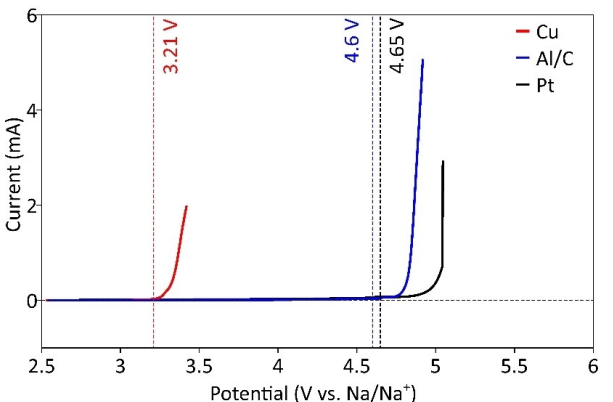
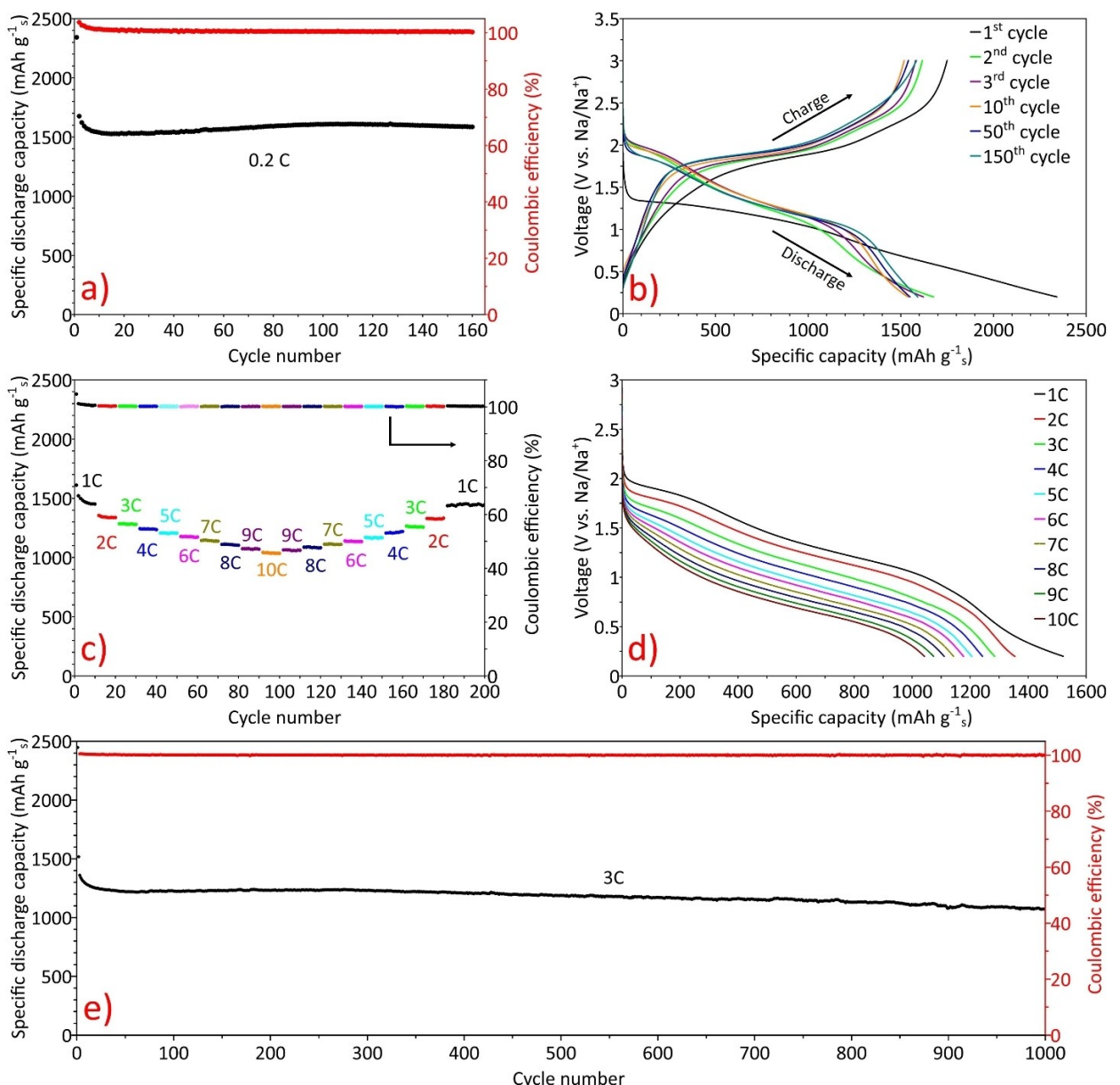


Figure 1. Stability of the electrolyte vs. oxidation as determined by LSV at a scan rate of  $2 \text{ mV s}^{-1}$  with Pt, Cu, and Al/C and Na, both as a reference and counter electrode.

avoided. Fourier-transform infrared spectroscopy (FTIR) shows the cyclization chemistry and sulfur incorporation during SPAN synthesis (Figure S3).

Different electrochemical tests were performed to evaluate the compatibility of the electrolyte with the Na anode and the SPAN cathode. First, galvanostatic cycling tests were conducted with Swagelok-type cells to assess the performance and electrochemical properties of Na-SPAN batteries. Cells were cycled between 0.2–3 V vs.  $\text{Na}/\text{Na}^+$  at alternating C rates. Figure 2a and Figure 2b show the galvanostatic cycling of the cell and the corresponding voltage curve at a C-rate of 0.2 C ( $340 \text{ mA g}^{-1}$ ). Notably, the experimentally determined capacity of the Na-SPAN cell ( $> 1500 \text{ mAh g}^{-1}$ ) is near the theoretical capacity of the final discharge product  $\text{Na}_2\text{S}$ , indicating sulfur is reduced to sulfide ( $\text{S}^{2-}$ ). Also, the capacity decay was as low as 0.033% per cycle, resulting in good reversibility of the system with virtual 100% coulombic efficiency as calculated from the ratio of discharge over charge capacities at the corresponding cycle. The voltage vs. capacity curve provides insights into the redox reactions and the corresponding potential plateaus (Figure 2b). The first complete discharge curve shows the highest capacity of  $2341 \text{ mAh g}^{-1}$ , attributable to electrolyte decomposition and SEI formation.<sup>[33]</sup> The capacity loss and voltage hysteresis in the first cycle is caused by irreversible reactions occurring at the anode and the poor electrical contact between SPAN and the carbon particles.<sup>[34]</sup> The overall capacity decreases slightly at the beginning of the cycling but fully recovers up to the 50<sup>th</sup> cycle, which indicates that the activation process occurred in the cathode during continuous cycling. During the 2<sup>nd</sup> discharge, the plateau shows a two-step reduction reaction at 1.84 V and 1.08 V (Figure 2b, green curve), corresponding to the formation of Na polysulfides ( $\text{Na}_2\text{S}_x$ ;  $2 \leq x \leq 4$ ) and  $\text{Na}_2\text{S}$ , respectively.<sup>[35]</sup> Due to the sluggish redox kinetics of  $\text{Na}_2\text{S}$ , a steeper curve appears at the end of the discharge plateau, indicative for slow solid-state reaction kinetics.

A similar deep discharge cut-off potential (0.1 V) was already reported for Na–S batteries based on an FEC-containing electrolyte and also in hybrid Na-ion-sulfur cells.<sup>[36]</sup> As outlined



**Figure 2.** Electrochemical performance of a  $\text{Na}[\text{B}(\text{hfip})_4]$ -based electrolyte in a Na-SPAN cell, a) galvanostatic cycling stability (black) and coulombic efficiency (red) at 0.2 C for 160 cycles; b) charge/discharge voltage profiles at 0.2 C during the 1<sup>st</sup> (black), 2<sup>nd</sup> (green), 3<sup>rd</sup> (purple), 10<sup>th</sup> (orange), 50<sup>th</sup> (blue) and 150<sup>th</sup> cycle (light blue); c) rate performances of the cathode ranging from 1 C to 10 C; d) voltage profiles at various C rates (1 C – 10 C) extracted from the rate capability test (Figure 2c); e) long-term galvanostatic cycling stability (black) and coulombic efficiency (red) at 3 C ( $5.025 \text{ A g}^{-1}$ ) over 1000 cycles.

earlier, the FEC additive plays an important role in stabilizing the anode surface, thereby preventing undesirable side reactions.<sup>[29,37]</sup>

Figure 2c and Figure 2d show the high-rate capability of Na-SPAN cells with different current densities ranging from 1–10 C and their respective voltage profiles. Capacities of 1450, 1337, 1279, 1235, 1204, 1172, 1138, 1102, 1069, 1034 mAh g<sup>-1</sup> were obtained at 1, 2, 3, 4, 5, 6, 7, 8, 9, and 10 C, respectively, with virtually 100% coulombic efficiency. Upon returning to a discharge rate of 1 C after 180 cycles, the discharge capacity almost fully restored, demonstrating excellent stress endurance of the SPAN cathode. The cell also exhibits exceptionally good rate performance at a high current density of 10 C, maintaining

1034 mAh g<sup>-1</sup>. The high capacity at higher current, e.g. at  $16.75 \text{ A g}^{-1}$ , is a result of the high conversion rate both during charging and discharging. To the best of our knowledge, such high capacity and cycle stability of a Na-S cell have not been reported before.

A long-term cycling test (Figure 2e) was conducted with a high current density of  $5.025 \text{ A g}^{-1}$  (3 C). The cell showed stable cycling over 1000 cycles while maintaining a high coulombic efficiency of virtual 100%. The Na-SPAN cell displayed an initial stable capacity of 1360 mAh g<sup>-1</sup> and maintained a capacity of 1072 mAh g<sup>-1</sup> at the end of the 1000<sup>th</sup> cycle with only 0.021% capacity decay per cycle. High reversibility and high capacity for longer cycling ascertain that

the electrolyte is compatible with the SPAN cathode. Commercially available salts such as sodium bis(trifluoromethylsulfonyl) imide (NaTFSI) and sodium trifluoromethanesulfonate (NaOTf) were compared with NaB(hfip)<sub>4</sub> to demonstrate the potential of salts with a WCA in Na–S batteries. Figure S4a and Figure S4c show a comparison of long-term cycling and rate capability of cells based on NaB(hfip)<sub>4</sub>, NaTFSI and NaOTf, respectively. Overall, cells based on NaB(hfip)<sub>4</sub> show high capacity, stable capacity retention at an extremely high C-rate, and low overpotential (Figure S4b).

To assess the electrolyte compatibility with the sodium anode, a cycling test was carried out by assembling symmetrical Na||Na cells (Figure 3a). Current density and capacity

were maintained at 0.565 mA cm<sup>-2</sup> and 0.285 mAh cm<sup>-2</sup>, respectively. The symmetric cells showed stable plating and stripping for at least 280 h. The initial perturbation in voltage during the first few Na-dissolution and -deposition steps are attributable to some electrolyte decomposition and SEI formation.<sup>[38]</sup> In the first few cycles, the deposition/dissolution overpotential (Figure 3b) of the cell reached 0.27 V/0.28 V, decreasing to 0.19 V and 0.13 V, respectively, at the end of the 280<sup>th</sup> cycle. This decrease in overpotential points towards low activation energy needed for Na-deposition and -dissolution. Electrochemical impedance spectroscopy (EIS) of the symmetrical cells during cycling was used to get insight into the origin of the cell resistance. During the initial stage open-circuit voltage (OCV)

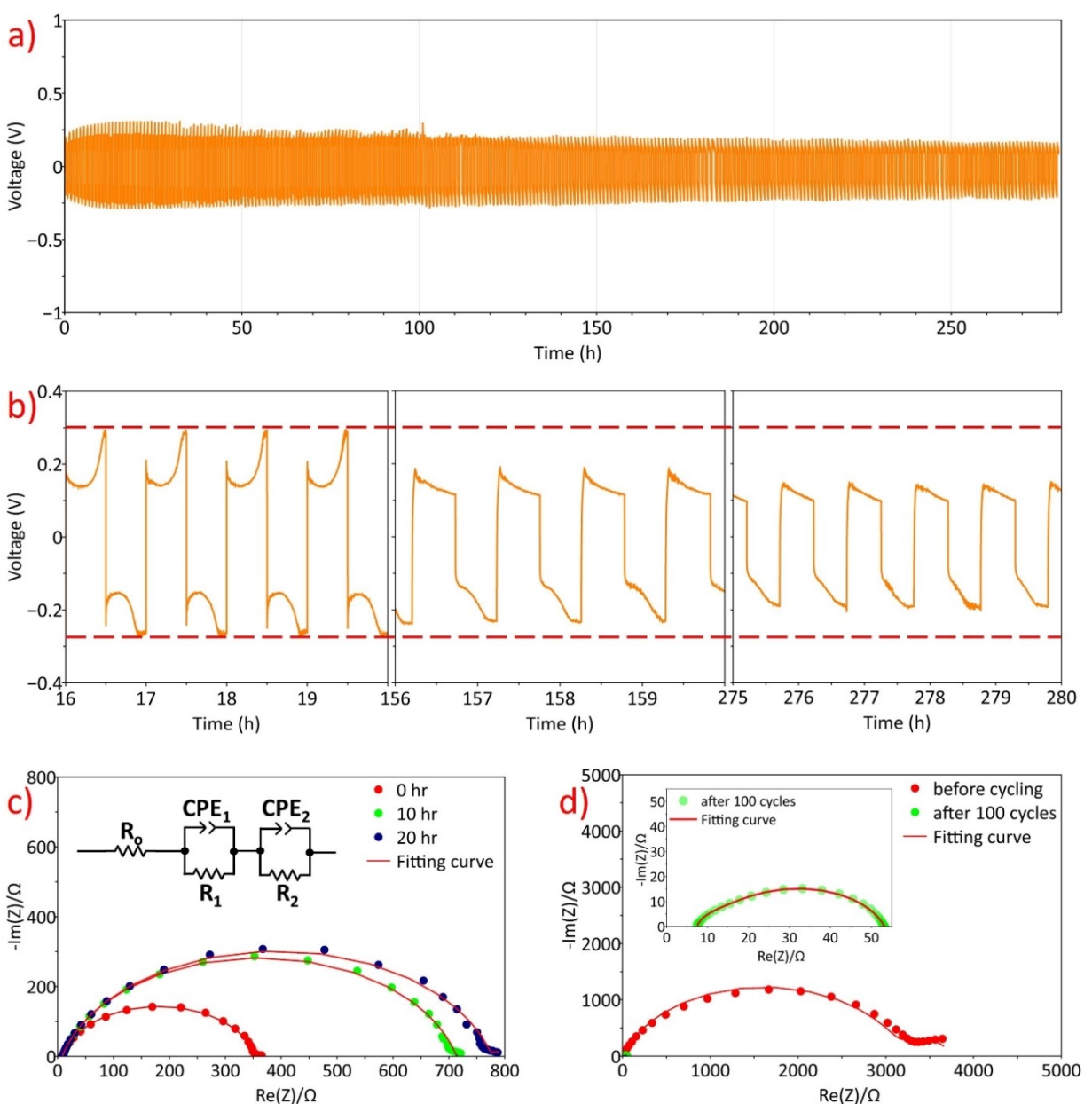


**Figure 3.** Electrochemical measurements of a symmetric Na||Na cell, a) Galvanostatic cycling voltage profiles at 0.565 mA cm<sup>-2</sup> (0.285 mAh cm<sup>-2</sup>); b) overpotential voltage profile at various times; c) impedance spectroscopy of a symmetric Na||Na cell at different OCV period (0<sup>th</sup> (red), 10<sup>th</sup> (green), 20<sup>th</sup> (blue)) (inset: equivalent circuit model); d) impedance before cycling (red) and after 100 cycles (green) (inset: zoom-in picture of impedance after 100 cycles).

period, the cell resistance increased due to the formation of the passivation (SEI) layer on the sodium surface. Freshly prepared cells showed a surface resistance (Figure 3c) of  $350\ \Omega$ ,  $702\ \Omega$ , and  $768\ \Omega$  after 0 h, 10 h and 20 h, respectively. This increase in cell resistance is directly related to the increase in SEI layer thickness with time. The equivalent circuit model used to fit the impedance data (shown in the inset of Figure 3c) contains  $R_0$ , two constant phase elements CPE<sub>1</sub> and CPE<sub>2</sub> connected parallelly to the respective resistor ( $R_1$ ,  $R_2$ ), with the two pairs ( $i=1,2$ ) in series. The electrolyte/bulk resistance ( $R_0$ ) together with the surface resistance ( $R_1+R_2$ ) describes both the SEI layer formation and charge-transfer resistance. Constant phase elements (CPE<sub>1</sub> and CPE<sub>2</sub>) are used to describe the capacitance of the electrochemical double layer. Diffusion of  $\text{Na}^+$  through the SEI layer at low frequency was avoided to fit the model accurately. Figure 3d shows the impedance of a symmetric  $\text{Na}||\text{Na}$  cell before the first cycle and after 100 cycles. Before cycling, the cell possesses a considerable surface resistance of  $3221\ \Omega$ . However, after 100 cycles, a dramatically reduced surface resistance of  $46.6\ \Omega$  was observed, attributable to an increase of the anode's surface area. This decrease in surface resistance suggests that the subsequent breakage and reformation of the SEI layer results in a larger surface area, which in turn helps to decrease the energy needed for stripping and plating. The rate performance of the symmetric cells was measured by applying current densities of 0.5, 1, 2, 3, and  $4\ \text{mA cm}^{-2}$  (Figure S5). A stable overpotential of 0.27, 0.31, 0.35 and 0.39 V, respectively, was observed for each current density. Only at higher current density ( $4\ \text{mA cm}^{-2}$ ), the overpotential increases rapidly, pointing towards the formation of an unstable SEI layer.<sup>[39–40]</sup>

### 2.3. Impact of Discharge Cut-Off Potential on the Electrochemical Stability of the Cell

The oxidation and reduction potential as well as the reversibility and electrolyte stability of a Na-SPAN cell were deduced from CV applying a low scan rate of  $0.1\ \text{mVs}^{-1}$ .<sup>[41]</sup> Concomitantly, the CV curves provide insights into the reaction kinetics based on the voltage applied and the corresponding current

density. The CV curves displayed in Figure 4a and Figure 4b reveal major differences during the sodiation/desodiation process when the DCP limits were fixed to 0.2 V and 0.5 V, respectively. During the first cycle applying a DCP of 0.2 V, two cathodic peaks are observed at 1.12 V and 0.51 V; these are shifted to higher potential, i.e. to 1.84 V and 1.08 V in the subsequent cycle. Similarly, applying a DCP of 0.5 V, one single reduction peak, though at a lower voltage (0.96 V), is observed during the first cycle. In a subsequent cycle, this peak shifted to 1.79 V and a second weak peak is observed at 1.25 V. The peak shifts during the second cycle go along with a considerable reduction in the polarization of the electrodes during cycling. During discharge, the peak at higher potential with both DCPs is attributable to the formation of  $\text{Na}_2\text{S}_x$  from SPAN, while the second peak indicates the formation of a mixture of  $\text{Na}_2\text{S}_2$  and  $\text{Na}_2\text{S}$ .<sup>[42]</sup> Upon charging,  $\text{Na}_2\text{S}$  is reconverted into polysulfides ( $-\text{S}_x-$ ) at ca. 1.9 V and all sulfur is bound to SPAN in the fully charged state above 2.28 V vs.  $\text{Na}/\text{Na}^+$ .<sup>[34,43]</sup> Elemental analysis (Table S2) allows for calculating an atomic ratio between carbon and sulfur, revealing that SPAN contains  $\text{C-S}_x$  bonds with  $x=3$  on average. Based on the atomic ratio between C and S, it can well be assumed that during discharge the intermediary-formed  $\text{S}_x$ -species predominantly exist in form of short-chain Na-polysulfides  $\text{Na}_2\text{S}_x$  ( $2 \leq x \leq 3$ ). The main anodic peak current (2<sup>nd</sup> cycle, Figure 4a) at a DCP of 0.2 V (0.45 mA) is higher compared to the one at a DCP of 0.5 V (2<sup>nd</sup> cycle, 0.29 mA, Figure 4b). This can be explained by a high conversion rate during oxidation at low DCP. It is also reasonable to assign the small anodic peak at 2.32 V to the final conversion reaction to  $\text{C-S}_x$ . Since the same cathodic peak current is observed at both DCPs, very similar electrode kinetics must exist during the reduction of sulfur.

Next, the influence of different DCPs on mass transfer during cycling was investigated by CV applying different scan rates (Figure 5a, Figure 5b). Both graphs show that an increase in the scan rate results in an increase in the peak current. With increasing scan rate, the cathodic and anodic peaks shift towards a more negative and more positive potential (i.e., overpotential), respectively, pointing towards a mixed mass transfer mechanism comprising both a diffusion-controlled and a charge-transfer controlled process.<sup>[44]</sup> At higher scan rates and

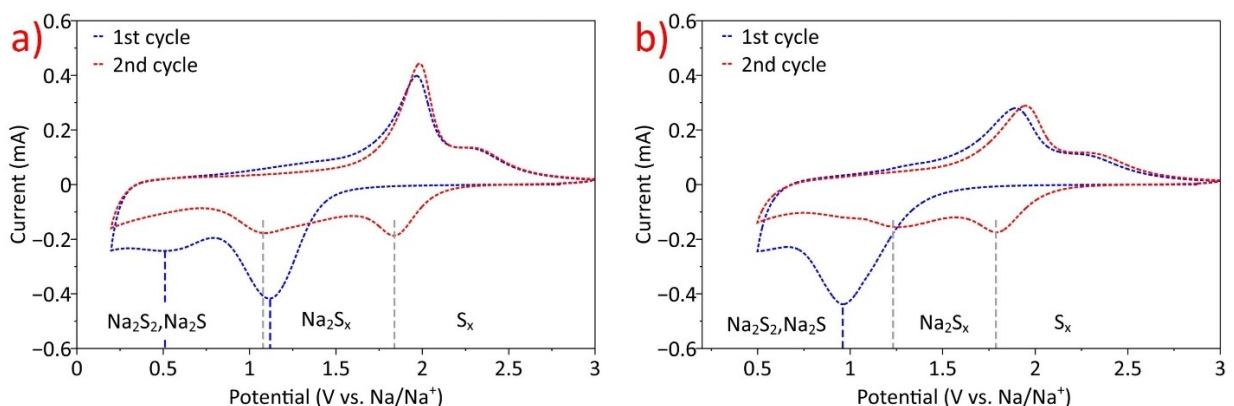
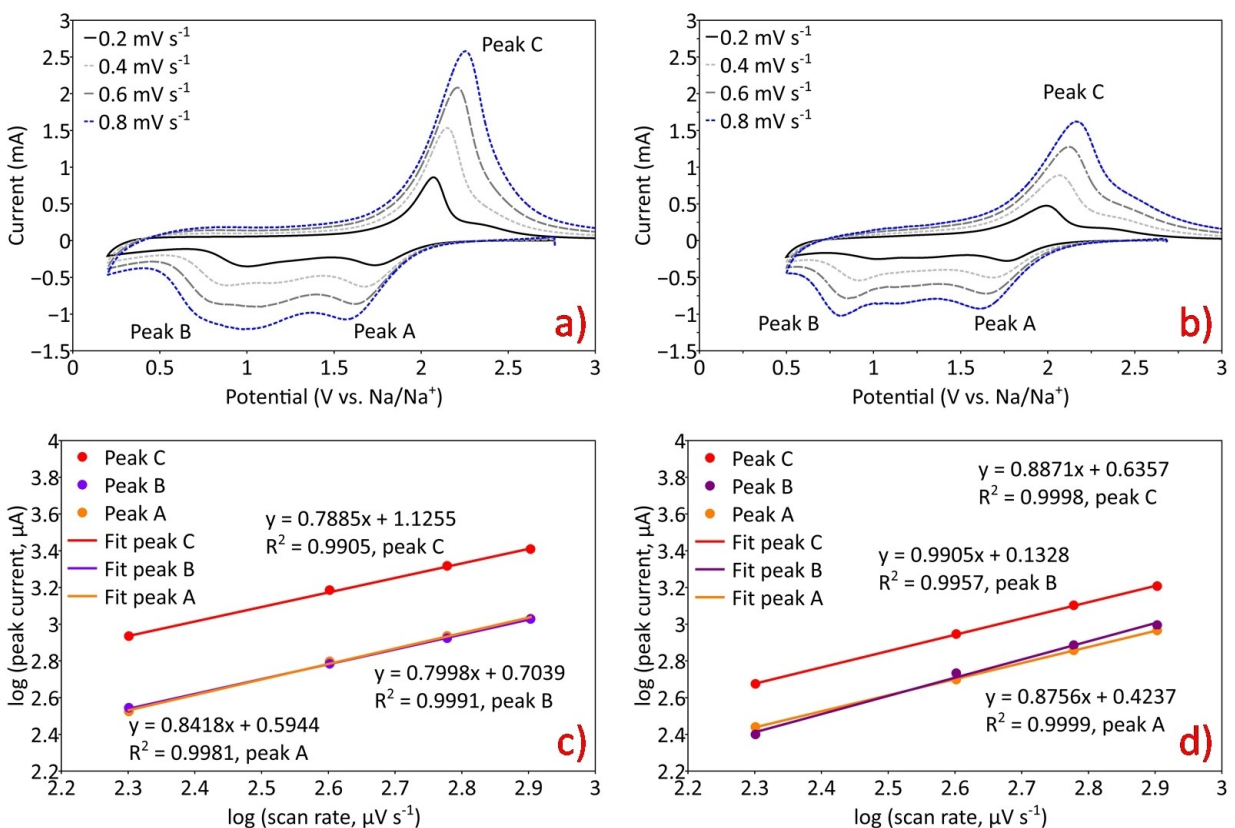


Figure 4. Cyclic voltammograms of a Na-SPAN cell recorded at the scan rate of  $0.1\ \text{mVs}^{-1}$  with different voltage windows, a) 0.2–3 V; b) 0.5–3 V.



**Figure 5.** Cyclic voltammograms of Na-SPAN cells with different cut-off potentials, a) 0.2–3 V; b) 0.5–3 V at varying scan rates. Double logarithmic plots of current vs. scan rate for (peak A (orange), peak B (purple), peak C (red)), c) 0.2–3 V; and d) 0.5–3 V.

a DCP of 0.2 V, despite having a wide reduction potential at peak B, the current increases significantly compared to a DCP of 0.5 V (Figure 5a and Figure 5b). We tentatively ascribe this to a predominant solid-state conversion of intermediary Na-polysulfides into Na<sub>2</sub>S.<sup>[45–46]</sup> At a higher scan rate (0.8 mV s<sup>-1</sup>), CV measurements with a DCP of 0.5 V show a larger potential gap between the main anodic and cathodic peak (157 mV) than CV measurements carried out at a DCP of 0.2 V (143 mV). An increase in the reduction onset potential and a decrease in the oxidation onset potential point towards lower polarization and accelerated polysulfide conversion at the peak voltage.<sup>[47]</sup> Vice versa, an insufficient conversion of sulfur leads to a lower anodic peak current (peak C, Figure 5b) at a DCP of 0.5 V, whereas a sharp peak at a DCP of 0.2 V is a result of high conductivity and high conversion (Peak C, Figure 5a). The oxidation peak at 2.35 V becomes insignificant as the scan rate increases, suggesting mass transfer limitations.

Since the DCP is of particular interest in this study, peak B in Figure 5a and Figure 5b was chosen to compare the reaction kinetics near the DCP. Using the Randles-Ševčík equation (Eq. S1),<sup>[48]</sup> the electrode processes can be determined through the relation between the peak current and the scan rate. Figure S6a and Figure S6b show a plot of the peak current, I (mA) vs. the square root of the scan rate,  $v^{1/2}$  ( $\text{V}^{1/2} \text{s}^{-1/2}$ ) with a good linear fit without intercepting origin, which is typical for a diffusion-controlled reaction.<sup>[49]</sup> The slope of the peak B at a DCP of 0.5 V (Figure S6b) was higher than the one at a DCP of 0.2 V

(Figure S6a), suggesting fast electrochemical kinetics. Nevertheless, a double logarithmic plot of  $I$  vs.  $v$  (Figure 5c and Figure 5d) shows a linear relationship, indicating that the redox reaction is also controlled by adsorption processes.<sup>[50]</sup> The gradient of the linear curve from the double logarithmic plot can be used to assess the contribution of the diffusion-controlled and surface-adsorption mass transfer process. Generally, mass transfer in a diffusion-controlled process is slower than the surface adsorption process. On the base of the semi-infinite diffusion-based Randles-Ševčík equation, the gradient close to 0.5 is indicative for a diffusion-controlled process. However, this slope can vary up to 1.0 for an adsorption process or a surface reaction, which is not uncommon for SPAN composites in which a redox reaction occurs with surface-bound S-moieties.<sup>[51–52]</sup> And indeed, for peak B, at a DCP of 0.2 V, the slope was 0.8 (Figure 5c), indicating mixed diffusion and interface-controlled mass transfer reactions. By contrast, for peak B at a DCP of 0.5 V (Figure 5d), a slope of 0.99 was observed, strongly suggesting that the redox reactions occur virtually solely with surface-bound C–S<sub>x</sub>/S–S species. Moreover, the slope near unity reconfirms that the reaction kinetics emerge from fast Na<sup>+</sup> ion transfer near the cut-off potential. This fast kinetics are a result of the fast reaction of electrode surface-adsorbed species that react immediately upon application of the potential step, whereas bulk species would have to diffuse to the electrode surface prior to reaction. This is also

supported by the sharp cathodic peak (Figure 5b) at a DCP of 0.5 V (peak B).

Figure 6a shows the galvanostatic cycling of two Na-SPAN cells at a DCP of 0.2 V and 0.5 V, respectively. Long-term battery tests with these two DCPs illustrate the stability of the cells and the high reversibility at 3 C. Even though both cells have high coulombic efficiencies of virtually 100%, cycling at a DCP of 0.5 V unveils a constant capacity decay from the beginning resulting in a specific discharge capacity of 541 mAh g<sup>-1</sup> after 500 cycles. This corresponds to an average capacity decay of 0.091% per cycle, which is almost four times higher than the average capacity decay observed at a DCP of 0.2 V (1187 mAh g<sup>-1</sup> at the end of the 500<sup>th</sup> cycle), which was 0.025% per cycle. This fast decay in capacity can be attributed to the formation of larger amounts of intermediary polysulfides such as S<sub>2</sub><sup>2-</sup>, S<sub>4</sub><sup>2-</sup> at a DCP of 0.5 V while mostly stable/inert Na<sub>2</sub>S forms at a DCP of 0.2 V, respectively. Figure 6b shows the 5<sup>th</sup> cycle of a charge-discharge curve at two different DCPs. Specific discharge capacities of 977 and 1314 mAh g<sup>-1</sup>, corresponding to the formation of Na<sub>2</sub>S<sub>2</sub> and Na<sub>2</sub>S,<sup>[53]</sup> respectively, were obtained at a DCP of 0.5 and 0.2 V. Since Na<sub>2</sub>S formation is sluggish, the voltage curve at a DCP of 0.2 V shows a small bump at 0.75 V (indicated by the dotted oval in Figure 6b) and then converges steeply at the end of the discharge. This behavior is well supported by the CV results suggesting that the broad peak at the end of the discharge (peak B, Figure 5a) is indeed related to the formation of Na<sub>2</sub>S. Using a DCP of 0.2 V also results in a reduced polarization, demonstrated by improved redox reactions during cycling as compared to a DCP of 0.5 V. In contrast to a DCP of 0.2 V in Figure 2c, the rate capability at a DCP of 0.5 V (Figure S7) results in a very sharp decrease in specific discharge capacity at a high current. At high current density (16.75 A g<sup>-1</sup>) mass transfer limitation rather leads to the formation of short-chain polysulfides than of Na<sub>2</sub>S. These short-chain polysulfides are responsible for the fast capacity decay since they can react with the carbonate-based solvent.<sup>[28,54-55]</sup>

Next, GITT was used to acquire kinetic data of the sodiation and desodiation process. The diffusion coefficient of Na<sup>+</sup> in the cathode at DCPs of 0.2 V and 0.5 V, respectively, can be

determined by applying current pulses followed by relaxation for a defined time (Figure S8a). Initial pre-formation cycles ensured full interface wetting of the electrodes of the Na-SPAN full cell with electrolyte. Figure 7a shows the sodiation and desodiation process for depths-of-discharge (DOD) and states-of-charge (SOC) between zero and 100%. The GITT equilibrium discharge curve shows two reduction potential plateaus, corroborating the results from CV and voltage vs. capacity curves (Figure 4a and Figure 6b). The relaxation voltage ( $V_{\text{relax}}$ ) (Figure S8b) during discharge shows a peak at 0.65 V and then gradually decreases. An increase in relaxation voltage near 0.5 V potentially points towards compositional inhomogeneity (Figure S8b), which can indeed be hypothesized by the surface-controlled reaction at a DCP of 0.5 V (Figure 5d).<sup>[56]</sup> This might initiate the conversion of surface-bound or adsorbed species at first, which eventually forces the inner domain species to react later during galvanostatic cycling. The diffusion coefficient of Na<sup>+</sup> ( $D_{\text{Na}^+}$ ) at different charge/discharge states can be determined by the transient voltage response theory using the Weppner and Huggins equation [Equation (S1)].<sup>[57]</sup> From Figure 7b, we deduce that at a discharge potential ( $U$ ) of 0.5 V the cell exhibits a  $D_{\text{Na}^+}$  value of  $2.6 \cdot 10^{-12} \text{ cm}^2 \text{ s}^{-1}$ . On the other hand, a  $D_{\text{Na}^+}$  value of  $4.7 \cdot 10^{-13} \text{ cm}^2 \text{ s}^{-1}$  was obtained at  $U = 0.2 \text{ V}$ , which is about one order of magnitude lower than at  $U = 0.5 \text{ V}$ . This higher diffusion coefficient at a discharge potential of 0.5 V supports a surface-controlled reaction as suggested by the double logarithmic plot (peak B, Figure 5d). From the consolidated data on diffusion,  $D_{\text{Na}^+}$  at a discharge potential of 0.2 V is the lowest in the entire discharge process. One can speculate that Na<sub>2</sub>S crystals that form upon discharge to 0.2 V block the ion channels, thereby impeding the diffusion of Na<sup>+</sup> into the cathode. Figure 7c also shows that during charging high diffusion values for Na were noticed at 2.2 V ( $D_{\text{Na}^+} = 3.6 \cdot 10^{-12} \text{ cm}^2 \text{ s}^{-1}$ ), indicating intermediate polysulfide conversion (peak C, Figure 5a and Figure 5b).

EIS at different charge and discharge voltages during cycling provides further evidence that Na<sub>2</sub>S formation is responsible for the decrease in  $D_{\text{Na}^+}$ . As can be seen in Figure S9a, the charge transfer resistance ( $R_{\text{ct}}$ ) decreases during charging due to the fact that Na<sub>2</sub>S/Na<sub>2</sub>S<sub>2</sub> are converted back to

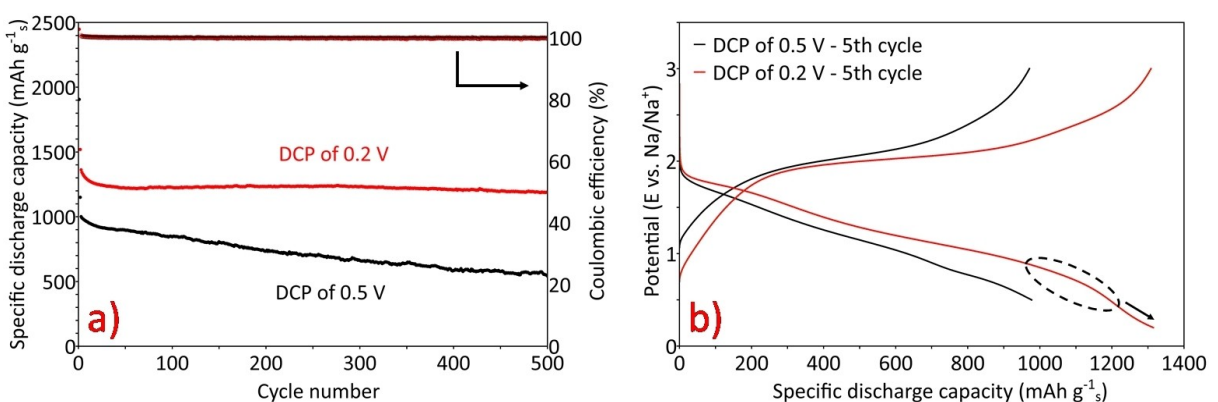
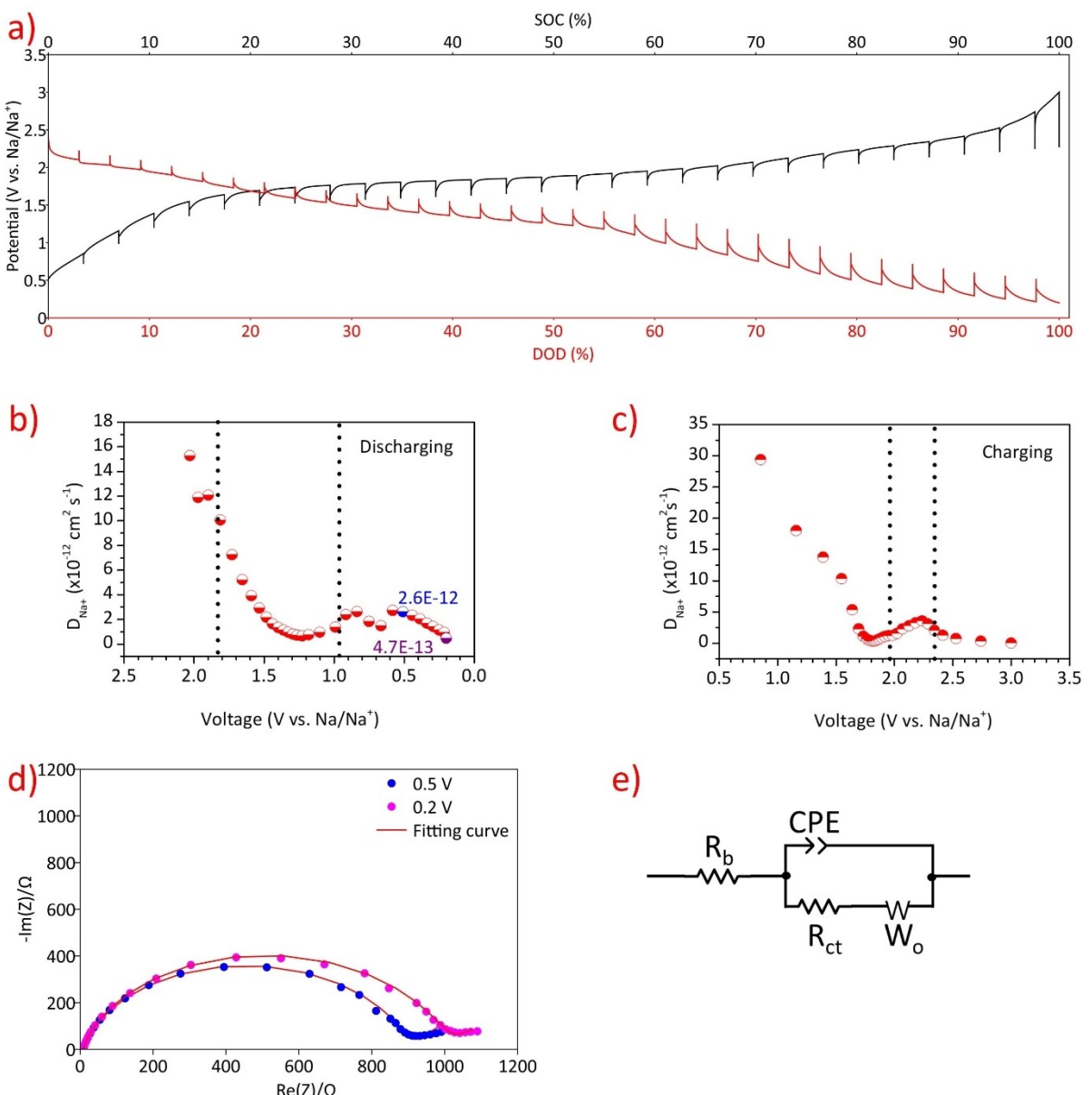


Figure 6. Galvanostatic cycling stability of a Na-SPAN cell (at 3 C) with two different DCP's, a) 0.2 V (red), 0.5 V (black), and b) the corresponding voltage profiles (charging and discharging) after the 5<sup>th</sup> cycle (dotted oval shows voltage bump at 0.75 V).



**Figure 7.** a) GITT pulses applied for 20 min at 0.1 C followed by 2 h relaxation. b, c) calculated diffusion coefficient at various potentials (b) during discharge (the values for 0.5 V and 0.2 V are indicated in blue and purple, respectively) and c) during charging, d) EIS of the discharged cathode at 0.5 V (purple) and 0.2 V (pink) and e) their equivalent circuit model ( $R_b$ -bulk resistance, CPE-constant phase element,  $R_{ct}$ -charge transfer resistance,  $W_o$ -Warburg impedance).

polysulfides and then to SPAN-bound sulfur, C-S<sub>x</sub>. By contrast, the electrolyte or bulk resistance ( $R_b$ ) of the cell is almost the same (8.1 Ω), both during charge and discharge. Discharge of the cell leads to an increase in  $R_{ct}$  since C-S<sub>x</sub> moieties are converted into electronically insulating solid Na<sub>2</sub>S (Figure S9b). The impedance of two voltage points at 0.5 V and 0.2 V during discharge and their corresponding equivalent circuit are shown in Figure 7d and Figure 7e. Impedance at 0.5 V shows a lower  $R_{ct}$  (884.6 Ω) than at 0.2 V ( $R_{ct}$  = 993.3 Ω, Table 1). This difference in impedance can be attributed to the comparably large amount of polysulfides, which have a lower  $R_{ct}$  than electrically insulating solid Na<sub>2</sub>S, which accumulates on the cathode, leading to poor charge transfer of the ions.

**Table 1.** Bulk resistance ( $R_b$ ) and charge transfer resistance ( $R_{ct}$ ) of Na-SPAN cell at a different discharge potential.

Discharge voltage [V]	$R_b$ [Ω]	$R_{ct}$ [Ω]
0.5	8.1	884.6
0.2	8.1	993.3

To evaluate the surface species formed on the cathode after cycling, ex situ XPS measurements were carried out under ultra-high vacuum conditions. Figure 8a-d and Table 2 show the S 2p spectra and binding energies of four separate SPAN cathodes in the pristine, charged, and two discharged states (DCP = 0.5 V and 0.2 V). Due to spin-orbit splitting, every sulfur species exhibits a 2p<sub>3/2</sub> and 2p<sub>1/2</sub> component. In the following,

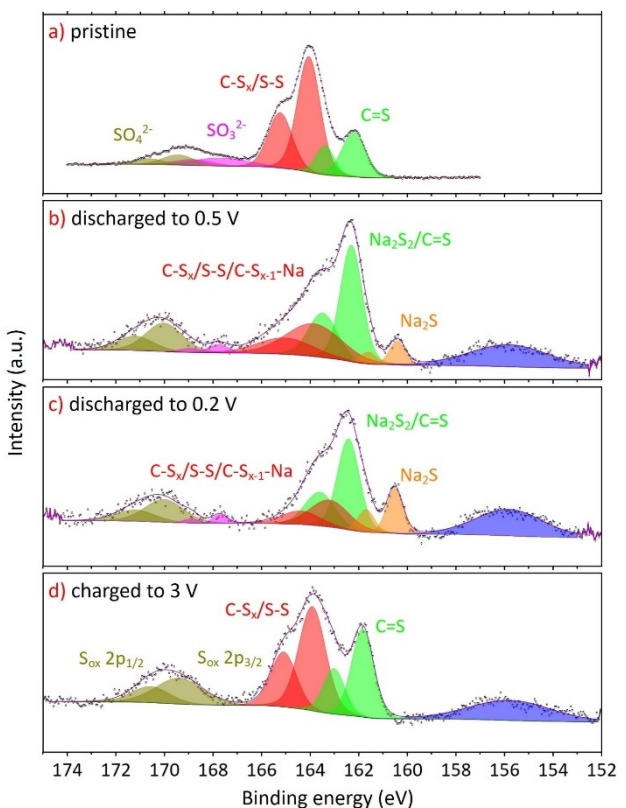


**Figure 8.** Sulfur S 2p ex situ XPS spectra of SPAN cathodes at different states (from top to bottom): pristine, discharged to 0.5 V, discharged to 0.2 V and charged to 3 V.

**Table 2.** Binding energies [eV] of the S 2p<sub>3/2</sub> species observed in pristine, charged and discharged cathodes.

	Na <sub>2</sub> S Na <sub>2</sub> S <sub>2</sub>	C=S, C-S <sub>x</sub> , S-S, C-S <sub>x</sub> -Na	SO <sub>3</sub> <sup>2-</sup> SO <sub>x</sub>	SO <sub>4</sub> <sup>2-</sup>	S <sub>ox</sub>	
Pristine	–	162.2	164.0	167.7	169.5	–
Charged 3 V	–	161.8	163.9	–	–	169.4
Discharged 0.5 V	160.4	162.3	163.7	167.8	169.9	–
Discharged 0.2 V	160.5	162.4	163.3	167.7	169.9	–

we only discuss the position of the S 2p<sub>3/2</sub> peaks (note that the fitted components for both angular momenta are included in the figure). The pristine SPAN cathode (Figure 8a) showed the typical signals for C=S, C-S<sub>x</sub>/S-S bonds. The S 2p<sub>3/2</sub> signals at 162.2 eV can be assigned to C=S and the peak at 164.0 eV can be assigned to S-S/C-S<sub>x</sub> moieties.<sup>[11,35, 58]</sup> Sulfate or thiosulfate species are observed at 166–172 eV.<sup>[30,59–60]</sup> The charged cathode (Figure 8d) shows similar sulfur components except for the thiosulfates, which were probably oxidized to sulfate during charging.

Figure 8b and Figure 8c show the S 2p regions for discharged cathodes at 0.5 V and 0.2 V. The same chemical components for the two cathodes are visible although their relative intensities differ. It is obvious that a new component at the low binding energy side (160.5 eV) appears for the discharged cathodes. We relate this to the formation of Na<sub>2</sub>S.<sup>[43,61]</sup> Please note that the peak between 152 and 158 eV

observed on the cycled cathodes can be related to the Si 2 s signal, which stems from the glass fiber.<sup>[62]</sup>

The signal of Na<sub>2</sub>S, which formed upon discharge, is overlapping with the C=S signal (binding energy around 162 eV). Since we cannot exclude that parts of the SPAN did not react with the Na upon discharge it is impossible to discriminate between these two different species. The same holds true for the polysulfide species around 164 eV which might be bound to C or Na. However, a shift towards lower binding energies and an increase of the full width at half maximum for the cathode discharged to 0.5 V and 0.2 V might indicate that this peak contains different chemical species like C-S<sub>x-1</sub>-Na and C-S<sub>x</sub>/S-S. Nonetheless, it is clearly visible that the amount of Na<sub>2</sub>S (peak colored orange at 160.5 eV) for the sample discharged at 0.2 V is higher than for the sample discharged at 0.5 V (15.6% of the whole S 2p intensity for DCP of 0.2 V and 6.1% for DCP of 0.5 V). Figure S10 shows the absence of a Na–C bond, indicating that sodiation of carbon is not preferred even at a low DCP of 0.2 V.

Scanning electron microscopy (SEM) images (Figure S11a and Figure S11b) show the differences between a pristine and an SPAN cathode discharged to 0.2 V. The pristine cathode contains smaller particles with large pore space in-between. Poor dispersibility of carbon particles is visible in form of large agglomerates. The discharged cathode shows less pore space with larger crystals, indicating Na<sub>2</sub>S formation. Energy-dispersive X-ray spectroscopy (EDX) measurements (Figure S12) reveal a high intensity of the sulfur signal in the pristine cathode and high intensity of sodium in the discharged cathode. To detect any potential formation of elemental sulfur after charging, the SPAN cathode was cycled 10 times and then analyzed by powder X-ray diffraction (XRD). Figure S13a and Figure S13b show both pristine and cycled SPAN cathodes (10 cycles) with no sign of crystalline sulfur formation. A broad signal between 20=15° to 25° stems from the turbostratic structure of the carbon (002) backbone in carbonized PAN. A small reflection at 20=20.1° indicates the limited crystalline nature of Na-CMC (binder).<sup>[63]</sup> Orthorhombic S<sub>8</sub> (20=23°, 222) embedded in the PAN structure loses its crystallinity during sulfurization. From Figure S13c, it is evident that both the cycled and pristine samples showed no additional reflections that would indicate the formation of another crystalline phase. Notably, both pristine and cycled SPAN have a broad signal at 20=20°, however, its intensity is higher in the pristine sample than in the cycled cathode, indicating some structural changes of SPAN during the first discharge. Alternatively, differences in intensity can be attributed to differences in cathode binder distribution.

### 3. Conclusions

In summary, a cycle stable room temperature Na–S battery was developed using a Na anode, a SPAN cathode and a carbonate-based electrolyte containing the WCA salt Na[B(hfip)<sub>4</sub>]. The electrolyte based on 1 M Na[B(hfip)<sub>4</sub>] in EC : DMC + 13 wt. % FEC showed a high ionic conductivity of 6.1 mS cm<sup>-1</sup> and high

anodic stability of 4.6 V on an Al/C current collector. Na-SPAN cells employing a WCA-based electrolyte exhibited superior rate capability and delivered a discharge capacity of 1072 mAh g<sup>-1</sup> at 3 C (5.025 A g<sup>-1</sup>) after cycling for 1000 cycles. The GITT measurements revealed a high conversion from polysulfides to solid and non-conductive Na<sub>2</sub>S at 0.2 V compared to 0.5 V, which was confirmed by a lower diffusion coefficient of Na<sup>+</sup> ( $D_{\text{Na}^+}$ ) at lower potential (0.2 V). The favored formation of Na<sub>2</sub>S at a DCP of 0.2 V compared to a DCP of 0.5 V was also confirmed by XPS measurements. The capacity decay at a DCP of 0.5 V is likely a result of the reaction between the carbonate-based electrolyte with the polysulfides formed when the cell is cycled between 0.5–3 V. We strongly believe that the use of other non- or weakly-coordinating anions in RT Na–S batteries will open new directions in the development of high energy density, high capacity and fast-charging batteries.

## Experimental Section

### 3.1. Synthesis of Na[B(hfip)<sub>4</sub>]

A slightly modified synthetic protocol was used for the synthesis of Na[B(hfip)<sub>4</sub>].<sup>[26]</sup> 3.0 g (79 mmol) of NaBH<sub>4</sub> were placed in a Schlenk flask filled with 250 ml of DME and the solution was cooled to 0 °C. 56.0 g (333 mmol) of hexafluoroisopropanol were added dropwise over 1 h via a dropping funnel under constant stirring. After the addition was completed, the solution was warmed to room temperature and stirred for another 1 h. Then, the temperature was increased slowly to 40 °C until H<sub>2</sub> evolution seized. To ensure complete conversion, the solution was refluxed overnight under vigorous stirring and then cooled to room temperature. The solvent was removed under vacuum, pentane was added and co-evaporated twice to remove most of the DME. Finally, the salt was dried at room temperature under vacuum (10<sup>-3</sup> mbar) for 48 h and 24 h under ultra-high vacuum (10<sup>-9</sup> mbar) at 30 °C. NMR (CD<sub>3</sub>CN) and elemental analysis confirmed sufficient purity (see Figure S1, Figure S2 and Table S1).

### 3.2. Synthesis and Fabrication of SPAN Cathodes

1.5 g of poly(acrylonitrile) powder (PAN,  $M_w$ =150, 000 g/mol, Sigma-Aldrich, Germany) was placed inside a quartz tube containing sulfur (ca. 20 g, Carl Roth) and degassed with nitrogen. The tube was heated to 160 °C until all sulfur was molten. Next, the mixture was heated from room temperature to 550 °C for 3 h and then cooled to room temperature. A nitrogen flow of 200 L/h was applied during the entire process. The SPAN was then subjected to Soxhlet extraction in toluene for 48 h to remove all unreacted sulfur. Elemental analysis revealed a sulfur content of 38.18±0.17 wt. % (see Table. S2). Next, a cathode slurry was prepared by mixing SPAN, carbon super C65 (MTI Corporation, USA), and NaCMC binder (High viscosity, Sigma-Aldrich, Germany; 70:20:10, wt. %) in water using a planetary mixer (Thinky, Japan) at 2000 rpm for 5 min. The as-prepared slurry was coated on carbon-coated aluminum foil (16 µm, MTI Co., USA) with a wet thickness of 300 µm using doctor blading (Erichsen, Germany). The coating was dried overnight at 60 °C. Finally, cathodes 12 mm in diameter were punched out. The obtained average sulfur content per cathode was 0.6 mg.

### 3.3. Electrochemical characterization

Electrochemical tests were performed in Swagelok-type cells assembled in an Ar-filled glovebox (O<sub>2</sub>, H<sub>2</sub>O < 0.1 ppm). The electrolyte was prepared by dissolving 1 M Na[B(hfip)<sub>4</sub>] in EC : DMC (1:1, vol. : vol.) and 13 wt. % FEC in a vial under stirring overnight followed by filtration and storage over 4 Å molecular sieves. The ionic conductivity of the electrolyte was measured with an InLab Sensor Conductometer (Mettler Toledo). Freshly cut sodium was pressed and rolled on a polyethylene surface and then cut into 12 mm disks. The cell was assembled in the following order: sodium foil, 120 µl of electrolyte, two wetted Whatman glass fiber separators (Ø=13 mm), and the SPAN cathode.

Linear sweep voltammetry (LSV), cyclic voltammetry (CV), potentiostatic electrochemical impedance spectroscopy (PEIS), galvanostatic intermittent titration technique (GITT), and overpotential measurements were conducted using a Biologic VMP3 integrated frequency response analyzer (France). LSV was conducted in a three-electrode set-up applying a scan rate of 2 mVs<sup>-1</sup> with platinum, copper, and carbon-coated aluminum as working electrode and sodium as the reference and counter electrode. CV measurements were performed between 0.2–3 V and 0.5–3 V, respectively, using SPAN as working electrode and sodium as reference and counter electrodes. PEIS was performed at a constant voltage of 10 mV alternating current with frequencies ranging from 800 kHz to 100 mHz and the resulting impedance curves were fitted using the built-in Zfit library. GITT was performed by cycling the cells first at the C-rate of 0.5 for 5 cycles (0.2–3 V) followed by 0.1 C for 20 mins, followed by a 2 h relaxation period until the battery was fully charged/discharged. Symmetric Na|Na cells were used in overpotential measurements applying different current densities. Long-term cycling and rate performance testing of the cells was conducted on BasyTec XCTS-LAB systems (Germany). Galvanostatic cycling was performed at different C rates (1 C = 1672 mAh g<sup>-1</sup>) with a voltage window between 0.2–3 V vs. Na/Na<sup>+</sup>. Unless mentioned otherwise, all cells were subjected to one preformation cycle at 0.3 C before testing. Rate capability testing was performed at varying C rates with ten cycles each between 1 C–10 C. For the analysis of the cut-off voltage effect on cycling, two different discharge cut-off potentials were chosen, i.e., 0.2–3 V and 0.5–3 V, respectively.

### 3.4. Material Characterization

XPS measurements were carried out after cycling the SPAN cathode-based cells for 30 cycles. Cathodes were washed with dimethyl carbonate (DMC) to remove excess electrolyte and then dried under vacuum at 40 °C. The samples then were transferred to the XPS system via an argon-filled transfer box to avoid exposure to air. A Kratos Axis Ultra system mounted with a monochromatic Al K $\alpha$  X-ray source was used. High-resolution data were acquired with a pass energy of 20 eV. Peak fitting and calculation of the atomic concentrations of the sulfur were carried out using the CasaXPS processing software. For fitting the spin-orbit split of the S 2p<sub>3/2</sub> and 2p<sub>1/2</sub> peaks, the binding energy separation and area ratios were constrained to 1.18 eV and 2:1, respectively. SEM of the SPAN samples was performed with an Auriga-type field emission scanning electron microscope (Zeiss) equipped with EDX. XRD measurements were conducted on a Rigaku SmartLab using a 3 kW sealed Cu-tube (monochromatic K<sub>α1</sub> emission,  $\lambda_{\text{cu}}=1.5406 \text{ \AA}$ ) in the transmission mode.

## Acknowledgments

We thankfully acknowledge funding and support from the German Federal Ministry for Economic Affairs and Energy (BMWi, project no. S50400, FiMaLiS). We thank Mr. J.V. Musso and Mr. Peter Schützendübe (MPI) and Mr. Jean-Louis Hoslauer (XRD measurement - Institute of Inorganic Chemistry) for fruitful discussions and Mr. U. Hageroth from the German Institute of Textile and Fiber Research (DIFT) Denkendorf for the SEM measurements. Open Access funding enabled and organized by Projekt DEAL.

## Conflict of Interest

The authors declare no conflict of interest.

**Keywords:** sulfurated poly(acrylonitrile) (SPAN) · room-temperature sodium-sulfur battery · electrochemistry · weakly coordinating anions · X-ray photoelectron spectroscopy

- [1] B. Dunn, H. Kamath, J.-M. Tarascon, *Science* **2011**, *334*, 928.
- [2] L. Gaines, *Sustain. Mater. Technol.* **2014**, *1*–*2*, 2–7.
- [3] G. Nikiforidis, M. C. M. van de Sanden, M. N. Tsampas, *RSC Adv.* **2019**, *9*, 5649–5673.
- [4] P. Adelhelm, P. Hartmann, C. L. Bender, M. Busche, C. Eufinger, J. Janek, *Beilstein J. Nanotechnol.* **2015**, *6*, 1016–1055.
- [5] P. K. Nayak, L. Yang, W. Brehm, P. Adelhelm, *Angew. Chem. Int. Ed.* **2018**, *57*, 102–120; *Angew. Chem.* **2018**, *130*, 106–126.
- [6] Z. Yang, J. Zhang, M. C. Kintner-Meyer, X. Lu, D. Choi, J. P. Lemmon, J. Liu, *Chem. Rev.* **2011**, *111*, 3577–3613.
- [7] Y.-X. Wang, B. Zhang, W. Lai, Y. Xu, S.-L. Chou, H.-K. Liu, S.-X. Dou, *Adv. Energy Mater.* **2017**, *7*, 1602829.
- [8] R. Mukkabla, M. R. Buchmeiser, *J. Mater. Chem. A* **2020**, *8*, 5379–5394.
- [9] J. Wang, J. Yang, J. Xie, N. Xu, *Adv. Mater.* **2002**, *14*, 963–965.
- [10] J. Fanous, M. Wegner, J. Grimminger, M. Rolff, M. B. M. Spera, M. Tenzer, M. R. Buchmeiser, *J. Mater. Chem.* **2012**, *22*, 23240–23245.
- [11] M. Frey, R. K. Zenn, S. Warneke, K. Müller, A. Hintennach, R. E. Dinnebier, M. R. Buchmeiser, *ACS Energy Lett.* **2017**, *2*, 595–604.
- [12] J. Fanous, M. Wegner, J. Grimminger, Å. Andresen, M. R. Buchmeiser, *Chem. Mater.* **2011**, *23*, 5024–5028.
- [13] J. Fanous, M. Wegner, M. B. M. Spera, M. R. Buchmeiser, *J. Electrochem. Soc.* **2013**, *160*, A1169–A1170.
- [14] J. Xiang, Z. Guo, Z. Yi, Y. Zhang, L. Yuan, Z. Cheng, Y. Shen, Y. Huang, *J. Energy Chem.* **2020**, *49*, 161–165.
- [15] J. Ye, F. He, J. Nie, Y. Cao, H. Yang, X. Ai, *J. Mater. Chem. A* **2015**, *3*, 7406–7412.
- [16] T. Lebherz, M. Frey, A. Hintennach, M. R. Buchmeiser, *RSC Adv.* **2019**, *9*, 7181–7188.
- [17] S. Warneke, A. Hintennach, M. Buchmeiser, *J. Electrochem. Soc.* **2018**, *165*, A2093–A2095.
- [18] J. Wang, J. Yang, Y. Nuli, R. Holze, *Electrochim. Commun.* **2007**, *9*, 31–34.
- [19] M. S. Syali, D. Kumar, K. Mishra, D. K. Kanchan, *Energy Storage Mater.* **2020**, *31*, 352–372.
- [20] A. Shyamsunder, W. Beichel, P. Klose, Q. Pang, H. Scherer, A. Hoffmann, G. K. Murphy, I. Krossing, L. F. Nazar, *Angew. Chem. Int. Ed.* **2017**, *56*, 6192–6197; *Angew. Chem.* **2017**, *129*, 6288–6293.
- [21] K.-C. Lau, T. Seguin, E. Carino, N. Hahn, J. Connell, B. Ingram, K. Persson, K. Zavadil, C. Liao, *J. Electrochem. Soc.* **2019**, *166*, A1510–A1519.
- [22] J. T. Herb, C. A. Nist-Lund, C. B. Arnold, *ACS Energy Lett.* **2016**, *1*, 1227–1232.
- [23] H. Tokuda, M. Watanabe, *Electrochim. Acta* **2003**, *48*, 2085–2091.
- [24] S. Tsujioka, B. Nolan, H. Takase, B. Fauber, S. Strauss, *J. Electrochim. Soc.* **2004**, *151*, A1418–A1423.
- [25] H. Tokuda, S.-i. Tabata, M. A. B. H. Susan, K. Hayamizu, M. Watanabe, *J. Phys. Chem. B* **2004**, *108*, 11995–12002.
- [26] I. Krossing, *Comprehensive Inorganic Chemistry II (Second Edition): From Elements to Applications* **2013**, *1*, 681–705.
- [27] S. Bulut, P. Klose, I. Krossing, *Dalton Trans.* **2011**, *40*, 8114–8124.
- [28] J. Gao, M. A. Lowe, Y. Kiya, H. D. Abruna, *J. Phys. Chem. C* **2011**, *115*, 25132–25137.
- [29] X. M. Zhao, Q. Zhu, S. D. Xu, L. Chen, Z. J. Zuo, X. M. Wang, S. B. Liu, D. Zhang, *J. Electroanal. Chem.* **2019**, *832*, 392–398.
- [30] X. Xu, D. Zhou, X. Qin, K. Lin, F. Kang, B. Li, D. Shanmukaraj, T. Rojo, M. Armand, G. Wang, *Nat. Commun.* **2018**, *9*, 3870.
- [31] A. Bhide, J. Hofmann, K. A. Dürr, J. Janek, P. Adelhelm, *Phys. Chem. Chem. Phys.* **2014**, *16*, 1987–1998.
- [32] J. Kasnatscheew, B. Streipert, S. Röser, R. Wagner, I. Cekic Laskovic, M. Winter, *Phys. Chem. Chem. Phys.* **2017**, *19*, 16078–16086.
- [33] E. Markevich, G. Salitra, Y. Talyosef, F. Chesneau, D. Aurbach, *J. Electrochem. Soc.* **2017**, *164*, A6244–A6253.
- [34] S. Zhang, *Energies* **2014**, *7*, 4588–4600.
- [35] Z.-Q. Jin, Y.-G. Liu, W.-K. Wang, A.-B. Wang, B.-W. Hu, M. Shen, T. Gao, P.-C. Zhao, Y.-S. Yang, *Energy Storage Mater.* **2018**, *14*, 272–278.
- [36] A. K. Haridas, J. Heo, X. Li, H.-J. Ahn, X. Zhao, Z. Deng, M. Agostini, A. Matic, J.-H. Ahn, *Chem. Eng. J.* **2020**, *385*, 123453.
- [37] M. Liu, D. Zhou, Y.-B. He, Y. Fu, X. Qin, C. Miao, H. Du, B. Li, Q.-H. Yang, Z. Lin, T. S. Zhao, F. Kang, *Nano Energy* **2016**, *22*, 278–289.
- [38] Y. Lu, Z. Tu, L. A. Archer, *Nat. Mater.* **2014**, *13*, 961–969.
- [39] L. Qin, H. Xu, D. Wang, J. Zhu, J. Chen, W. Zhang, P. Zhang, Y. Zhang, W. Tian, Z. Sun, *ACS Appl. Mater. Interfaces* **2018**, *10*, 27764–27770.
- [40] G. Bieker, M. Winter, P. Bieker, *Phys. Chem. Chem. Phys.* **2015**, *17*, 8670–8679.
- [41] X. Huang, Z. Wang, R. Knibbe, B. Luo, S. A. Ahad, D. Sun, L. Wang, *Energy Technol.* **2019**, *7*, 1801001.
- [42] S. Ma, P. Zuo, H. Zhang, Z. Yu, C. Cui, M. He, G. Yin, *Chem. Commun. (Camb.)* **2019**, *55*, 5267–5270.
- [43] A. Y. S. Eng, D.-T. Nguyen, V. Kumar, G. S. Subramanian, M.-F. Ng, Z. W. Seh, *J. Mater. Chem. A* **2020**, *8*, 22983–22997.
- [44] F. Scholz, *Electroanalytical Methods*, Vol. 1, Springer, 2010.
- [45] D. Kumar, D. K. Kanchan, S. Kumar, K. Mishra, *Mater. Sci. Technol.* **2019**, *2*, 117–129.
- [46] I. Bauer, M. Kohl, H. Althues, S. Kaskel, *Chem. Commun. (Camb.)* **2014**, *50*, 3208–3210.
- [47] Y. Tao, Y. Wei, Y. Liu, J. Wang, W. Qiao, L. Ling, D. Long, *Energy Environ. Sci.* **2016**, *9*, 3230–3239.
- [48] X. Tao, J. Wang, C. Liu, H. Wang, H. Yao, G. Zheng, Z. W. Seh, Q. Cai, W. Li, G. Zhou, C. Zu, Y. Cui, *Nat. Commun.* **2016**, *7*, 11203.
- [49] A. K. Timbola, C. D. Souza, C. Soldi, M. G. Pizzolatti, A. Spinelli, *J. Appl. Electrochem.* **2007**, *37*, 617–624.
- [50] J.-j. Wu, *Int. J. Electrochem. Sci.* **2016**, *11*, 5165–5179.
- [51] Z. Li, J. Zhang, Y. Lu, X. W. Lou, *Sci. Adv.* **2018**, *4*, 1687.
- [52] J. Ding, H. Zhou, H. Zhang, L. Tong, D. Mitlin, *Adv. Energy Mater.* **2018**, *8*, 1701918.
- [53] X. Yu, A. Manthiram, *ChemElectroChem* **2014**, *1*, 1275–1280.
- [54] G. W. Luther, *Geochim. Cosmochim. Acta* **1991**, *55*, 2839–2849.
- [55] H. Zhang, T. Diemant, B. Qin, H. Li, R. Behm, S. Passerini, *Energies* **2020**, *13*, 836.
- [56] L. Li, R. Jacobs, P. Gao, L. Gan, F. Wang, D. Morgan, S. Jin, *J. Electrochem. Soc.* **2016**, *153*, 2838–2848.
- [57] W. Weppner, R. A. Huggins, *J. Electrochem. Soc.* **1977**, *124*, 1569–1578.
- [58] B. J. Lindberg, K. Hamrin, G. Johansson, U. Gelius, A. Fahlman, C. Nordling, K. Siegbahn, *Phys. Scr.* **1970**, *1*, 286–298.
- [59] C.-P. Yang, Y.-X. Yin, Y.-G. Guo, L.-J. Wan, *J. Electrochim. Soc.* **2015**, *137*, 2215–2218.
- [60] Q. Yang, T. Yang, W. Gao, Y. Qi, B. Guo, W. Zhong, J. Jiang, M. Xu, *Inorg. Chem. Front.* **2020**, *7*, 4396–4403.
- [61] S. Wei, S. Xu, A. Agrawal, S. Choudhury, Y. Lu, Z. Tu, L. Ma, L. A. Archer, *Nat. Commun.* **2016**, *7*, 11722.
- [62] R. Aghaei, A. Eshaghie, *J. Alloys Compd.* **2017**, *699*, 112–118.
- [63] A. Salama, M. El-Sakhawy, S. Kamel, *Int. J. Biol. Macromol.* **2016**, *93*.

Manuscript received: June 1, 2021

Revised manuscript received: June 24, 2021

Accepted manuscript online: July 14, 2021

Version of record online: July 28, 2021